Published as: *Nature*. 2013 August 8; 500(7461): 175–181.

# A visual motion detection circuit suggested by *Drosophila* connectomics

**Shin-ya Takemura**[1], **Arjun Bharioke**[1], **Zhiyuan Lu**[1,2], **Aljoscha Nern**[1], **Shiv Vitaladevuni**[1], **Patricia K. Rivlin**[1], **William T. Katz**[1], **Donald J. Olbris**[1], **Stephen M. Plaza**[1], **Philip Winston**[1], **Ting Zhao**[1], **Jane Anne Horne**[2], **Richard D. Fetter**[1], **Satoko Takemura**[1], **Katerina Blazek**[1], **Lei-Ann Chang**[1], **Omotara Ogundeyi**[1], **Mathew A. Saunders**[1], **Victor Shapiro**[1], **Christopher Sigmund**[1], **Gerald M. Rubin**[1], **Louis K. Scheffer**[1], **Ian A. Meinertzhagen**[1,2], and **Dmitri B. Chklovskii**[1]

[1]Janelia Farm Research Campus, HHMI, Ashburn, VA, USA

[2]Department of Psychology and Neuroscience, Dalhousie University, Halifax, NS, Canada

## Summary

Animal behavior arises from computations in neuronal circuits, but our understanding of these computations has been frustrated by the lack of detailed synaptic connection maps, or connectomes. For example, despite intensive investigations over half a century, the neuronal implementation of local motion detection in the insect visual system remains elusive. Here, we developed a semi-automated pipeline using electron microscopy to reconstruct a connectome, containing 379 neurons and 8,637 chemical synaptic contacts, within the *Drosophila* optic medulla. By matching reconstructed neurons to examples from light microscopy, we assigned neurons to cell types and assembled a connectome of the medulla's repeating module. Within this module, we identified cell types constituting a motion detection circuit and showed that the connections onto individual motion-sensitive neurons in this circuit were consistent with their direction selectivity. Our results identify cellular targets for future functional investigations, and demonstrate that connectomes can provide key insights into neuronal computations.

Vision in insects has been subject to intense behavioral[1], physiological[2] and anatomical[3] investigations, yet our understanding of its underlying neural computations is still far from complete. One such computation, ethologically highly relevant, is motion detection, which is thought to rely on the comparison between signals offset in space and time (Fig. 1a,b)[4–6].



Correspondence and requests for materials should be addressed to D.B.C. (mitya@janelia.hhmi.org) or I.A.M. (iam@dal.ca)..

***Supplementary Information*** is linked to the online version of the paper at www.nature.com/nature.

***Author Contributions*** D.B.C. and I.A.M. designed the research. Z.L., S.T. and R.D.F. prepared and imaged the sample. D.J.O., P.W., S.M.P., S.V., and W.T.K., under the guidance of D.B.C. and L.K.S., developed software for the reconstruction. S.T. annotated the micrographs, proofread the segmentation, and assembled the connectome, with the help of proofreaders (S.T.2, K.B., L.C., O.O., M.A.S., V.S., and C.S.) supervised by P.K.R and J.A.H. A.N. and G.M.R. provided and A.N. analyzed light microscopy images. L.K.S. and A.B. performed data analysis and T.Z. aided in visualization. A.B. and D.B.C. studied the motion detection circuit. A.B., D.B.C, I.A.M., and L.K.S. wrote the paper, with contributions from S.T. and A.N.

***Author Information*** Reprints and permissions information is available at www.nature.com/reprints. The author declare no competing financial interests.

Yet, despite being the focus of theoretical and experimental investigations for over half a century[7], the exact mechanism underlying this computation remains a mystery. A central impediment towards unravelling this mechanism has been our incomplete knowledge of the relevant neurons and synapses.

In the fly, visual processing begins in the optic lobe, composed of four retinotopically organized neuropils. Each is an array of repeating modules corresponding to the hexagonal lattice of ommatidia in the compound eye (Fig. 1c). Each module of the first neuropil, the lamina, contains a repeating circuit[8,9] receiving inputs from six photoreceptors detecting light from the same location in the visual field. The output cells of each lamina module project to a corresponding module of the second neuropil, the medulla (Fig. 1c). Each medulla module, called a column (Fig. 1d), is also thought to contain stereotypic circuits[10]. These columns, in turn, innervate two downstream neuropils, the lobula and lobula plate (Fig. 1c).

In which neuropil do motion detection circuits reside? The first neuropil with movement specific activity is the medulla[12]. Directly downstream of the medulla, lobula plate tangential cells (LPTCs) integrate local motion signals to generate responses to wide-field motion[13,14]. Thus, local motion responses should be computed at least partly within the stereotypical circuits of the medulla columns. To date, however, these have proven impossible to map at a synaptic level, frustrating investigation of the mechanism underlying motion detection.

## Semi-automated connectome reconstruction

To provide a reliable foundation for computational modeling and identify targets for electro/optophysiological recordings, we attempted a complete, dense reconstruction of the chemical synaptic connectivity within the medulla using electron microscopy (EM), the gold standard of neuroanatomy[15]. Given the time-consuming nature of such reconstructions, we wanted to determine the smallest medulla volume, reconstruction of which would allow us to identify a circuit underlying the computation of local motion. Both directional turning responses[16] and electrophysiological responses in LPTCs[17] can be elicited in flies by sequential stimulation of two photoreceptors corresponding to adjacent points anywhere in the visual field[18]. This suggests that some repeating component of the motion detecting circuit must be present within any two adjacent medulla columns. We therefore decided to reconstruct all the synaptic connections among neurons within a single *reference* column, as well as all the connections between the reference column and neurons within six nearest-neighbor columns (Fig. 1d).

Since manual reconstruction of even a seven-column volume would be prohibitively time-consuming[19], we developed a semi-automated reconstruction pipeline[20] and applied it to the medulla volume (Fig. 2, Methods, Supplementary Data 1), reconstructing 379 cells (Supplementary Fig. 1 and Video 1).

To map our reconstruction onto the existing body of knowledge, we assigned these cells to previously proposed cell types[21] by comparing the shapes of reconstructed arbors (Supplementary Fig. 1) with those reported from light microscopy using Golgi impregnation

or genetic single-cell (GSC) labeling (Fig. 2e,f, Supplementary Methods). Since there were multiple reconstructed examples for almost all neuronal types (Supplementary Fig. 1, Supplementary Table 2), it was possible to characterize the common structural features of each type. In many cases, this allowed us to match unequivocally a reconstructed cell with a Golgi impregnate[21], for which it was then named (Supplementary Methods). However, there was also a subset of cell types for which a Golgi counterpart could not be found but which we validated using isomorphs from GSC labeling. We named these cell types Mi13, Mi14, Mi15, TmY14, Dm9, and Dm10 (Supplementary Fig. 2). In total, from the collection of 379 reconstructed cells (Supplementary Fig. 1) we were able to classify 290 of them into 56 cell types (Supplementary Table 2).

To reveal the connections between the 379 reconstructed neurons, we identified pre-and postsynaptic sites and assigned them to their respective parent cells. Within the reference column and its immediate surround, we annotated 10,093 presynaptic sites and 38,465 associated postsynaptic sites (3.8 ± 1.2, SD, per presynaptic site) (Fig. 2c, Supplementary Table 1). While presynaptic T-bars typically fell onto proofread profiles of neurons, postsynaptic sites usually fell onto isolated profiles, unassigned to any neuron. Thus, it was necessary to trace the dendrite containing each postsynaptic site back to a parent cell. This postsynaptic tracing was extremely challenging since *Drosophila* neuron dendrites branch elaborately and, indeed, can be thinner than the section thickness.

The challenging postsynaptic tracing led to (i) some erroneously identified synaptic contacts and (ii) a high fraction (~50%) of contacts that could not be traced to their parent neuron and were, therefore, unidentified. To increase our confidence in the identified contacts (i), we had two proofreaders trace every postsynaptic site (Methods), and only accepted into the connectome those contacts that both proofreaders identified independently. In contrast, it was not possible to experimentally reduce the number of unidentified contacts (ii). However, we were still able to construct a connectome valuable for inferring function because we found that, within the medulla, connections of high weight (i.e high number of synaptic contacts per connection) both capture a large fraction of the total connection weight and can be identified with high fidelity. Indeed, the distribution of connection weight in our connectome is heavy tailed (Fig.3b, inset, Supplementary Fig. 3), as has been found in other organisms[22,23]. Also, assuming that synapses are equally difficult to proofread, we found that any strong connection (with >5 synaptic contacts) will be identified with probability >95%. Therefore, in the resulting connectome, 8,637 synaptic contacts are precisely identified, and all strong connections are represented.

## The connectome module and its pathways

To identify pathways performing local computations such as motion detection, it was necessary to generate a more convenient abstraction of the full connectome. Since we expect that the circuits of interest repeat within each column, we extracted from the medulla connectome a periodic module of connections between identified cell types that arborize in every column. These include both so-called synperiodic cell types with single neurons in every column of the medulla[24], and cell types with multiple members within each column, which we term ultraperiodic. We do not include infraperiodic tangential or local amacrine-

like cells even if they have arborizations in every column because this cannot be determined unambiguously from our EM reconstruction (Supplementary Table 2). We utilized the existence of multiple representatives from adjacent columns within our EM reconstruction (Supplementary Fig. 1) to identify 25 cell types as synperiodic as well as two cell types, Tm3 and T4, as ultraperiodic (with 1.5 and 4 cells per column, respectively) (Supplementary Table 2). We termed these 27 cell types modular.

Assuming that connections between modular cells are stereotypical between columns, we constructed the repeating circuit module by finding all connections between these cell types (Methods). Unlike sparse reconstructions, the resulting connectome module (Fig. 3a) accurately captures not only the presence but also the absence of strong connections between any two cell types.

To determine which neurons could be involved in different local computations, we dissected the connectome module into three separate signal processing pathways, using both a clustering and a layout algorithm (Fig. 3). We recognized them as the previously identified pathways, those of L1, L2, and L3/R7/R8. The downstream targets of R7 and R8 have previously been implicated in color vision. Because color pathways are separated into differing columns receiving inputs from either pale or yellow ommatidia[27], we expect that they should rely on infraperiodic cell types omitted from our connectome module. Therefore, the fine structure of the L3/R7/R8 pathway will be revisited elsewhere.

The remaining L1 and L2 pathways signal visual contrast, and are implicated in motion detection[7,28–32]. Behavioral experiments and electrophysiological recordings confirm this role for L1 and L2: not only is each necessary for aspects of motion detection[32–34], but, among the cells postsynaptic to the photoreceptors R1–R6, both are also mostly sufficient[33,34] for the computation. However, L1 and L2 themselves lack directionally-selective responses[7,28]. Therefore, to search for motion detection circuit(s) within the connectome module, we examined the neurons downstream of L1 and L2 in more detail.

## Candidate motion detection circuit

Several lines of evidence indicate that motion information computed downstream of L1 and L2 is relayed to the lobula plate via cell types T4 and T5[28]. First, recordings from LPTCs in fruit flies with genetically silenced T4 and T5 demonstrate that at least one of these columnar cell types is necessary to detect direction selectivity[35]. Second, T4 and T5 cells in *Drosophila* each comprise four subtypes differentiated by the lobula plate layer in which their axons arborize[21]. Third, each of these four layers within the lobula plate exhibits activity in response to wide-field stimuli moving in a particular direction: downwards, upwards, backwards, and forwards (Fig. 4b,e), revealed by their uptake of deoxyglucose[12,30]. Finally, dendrites of LPTCs with different motion preference co-occupy the lobula plate layers corresponding to their directional preference [21] and, in addition, receive direct synaptic connections from T4 terminals[31]. Collectively, these data suggest that each subtype of T4 / T5 forms the output of motion detection circuits signaling a particular direction of motion.

Next, we argue that the direction-selective outputs of T5 and especially T4 are computed largely independently of each other. Consistent with stratum-overlap analysis in *Drosophila*[29] and large flies[28], our connectome (Fig. 3a,b) indicates that T4 belongs to the L1 pathway. Conversely, although we did not trace into the lobula, the dendrites of T5s co-occupy layers in the lobula with the axon terminals of neurons such as Tm1[21,28], Tm2[21], and Tm4[21], which belong to the L2 pathway (Fig. 3b). Electrophysiological[33] and behavioral[32] evidence indicate that L1 and L2 pathways in the connectome module (Fig. 3a,b) are computationally independent and correspond to ON and OFF pathways in the visual systems of vertebrates[33]. Further, most of the connections from the L2 pathway to the L1 pathway arrive via L5 (Fig. 3a), a cell type not implicated in motion detection[36]. Hence, we decided to search for a motion detection circuit downstream of L1 converging upon T4. This decision was made despite electrophysiological evidence showing a lack of direction selectivity in T4s[37], but since the completion of our work, has been supported by calcium imaging of T4s[38].

To identify candidate elements of a motion detection circuit bridging between L1 and T4, we took advantage of the fact that motion detection is both fast and robust to noise[17,18], and consequently should be implemented by both feedforward and strong connections. Our dense EM reconstruction identified five cell types with significant input from L1: Mi1, Tm3, L5, C2, and C3 (Fig. 3a). Cell types Mi1 and Tm3 are the two largest recipients of L1 input, together accounting for more than half of L1's synaptic contacts. In turn, Mi1 and Tm3 together contribute >80% of presynaptic inputs to T4 (including all inputs from both modular and non-modular cell types), thus forming the two strongest paths from L1 to T4. In contrast, cell type C3 contacts T4 with an order of magnitude fewer synapses than Mi1 and Tm3, suggesting that its contribution is far weaker. Finally, cell types L5 and C2 have no synapses directly with T4. These features lead us to suggest that Mi1 and Tm3 are the only possible substrates for robust, and fast motion detection within the L1 pathway.

## Anatomical receptive fields of T4 cells

To explore further if Mi1s and Tm3s converging upon T4s could constitute the two arms of a correlation-based motion detector (Fig.1a,b), we examined whether the motion axis defined by these inputs onto a particular T4 is consistent with its preferred direction, as measured by its outputs. This output preferred direction was determined for 16 T4 neurons by tracing their axons into the lobula plate and identifying their arborization layer[12,30] (Fig. 4b,e, 6b).

To compare the preference of T4 output with the motion axis arising from its inputs, we constructed the input motion axis by analyzing the numbers of contacts from individual Mi1 and Tm3 cells onto the T4 neuron in question. We found that each T4 receives inputs from several Mi1 and Tm3 neurons suggesting that, unlike the circuits in Fig. 1a and b, multiple points in the visual field provide inputs into each arm of the motion detector (Fig. 4a,b,e). This observation is supported by the structure of sampling units inferred from recordings in blowfly H1[39], which receives inputs from LPTCs[40]. We therefore needed to characterize the inputs to each T4 as Mi1- and Tm3-mediated receptive field components, mapped into the visual field. To do this, we traced synaptic connections from L1 terminals in 19 columns

(the reference column and surrounding 18 columns) to the downstream Mi1 and Tm3 cells and then from the Mi1 and Tm3 neurons onto T4s that receive input from the reference column (which also happen to number 19). The resulting receptive fields (Fig. 4a, Supplementary Fig. 4) show the T4 inputs mapped as if upon the L1 array and hence into the visual field.

For all T4s, the Mi1- and Tm3-mediated components of the T4 receptive field overlap substantially with one another (Supplementary Fig. 4). Indeed, the centers of mass of the two components are displaced less than one inter-ommatidial distance (Fig. 5a). However, for 15 of the T4s, this displacement is still significantly greater than would have been obtained by chance from tracing errors. Such a small displacement magnitude relative to the widths of the receptive fields agrees with prior evidence inferred from blowfly H1 recordings and has been justified theoretically[39].

Is the direction of displacement between the Tm3 and Mi1 receptive field components for a T4 neuron consistent with the neuron's directional preference as defined by the depth of its terminal axonal arborization in the lobula plate? Assuming that the direction of the displacement is determined from the Tm3 to Mi1 component centers of mass, Fig. 5b (top) shows that the direction of displacement agrees with the directional preference for three of the four lobula plate layers. The discrepancy in the direction of displacement and the front-to-back motion preference of T4s terminating in the fourth layer (Lp4) may be caused by neglected circuits contributing specifically to the responses of these T4 neurons. For example, behavioral evidence implicates C3 neurons in front-to-back motion detection[36], and, indeed, preliminary tracing results suggest that, despite C3s providing an order of magnitude fewer inputs to T4s than Mi1s or Tm3s, C3 neurons target Lp4 T4s preferentially.

Some of the discrepancy between the receptive field offset and the directional preference of individual T4s (Fig. 5a) innervating lobula plate layers 1 – 3 is probably caused by a systematic error in our reconstruction resulting from the finite size of the reconstructed region. Indeed, the discrepancy between the measured input displacement for a given T4 and its predicted direction preference correlates with the weighted fraction of missing L1 inputs onto Tm3s upstream of that T4 (Fig. 5b, bottom), supporting the view that the fields of peripheral T4s may not be fully reconstructed. In addition, some of the remaining variation in the offset orientation may also be real, given the observed 60° – 90° half-width of the tuning curves obtained through calcium imaging of individual T4 subtypes[38].

Our choice to measure displacement from Tm3 to Mi1 (and not in the reverse order) appears arbitrary without including information about delays and synaptic polarity (Fig. 1a,b). To estimate a possible conduction delay, we measured both the path length and the caliber of the main axon trunks that conduct signals along the Mi1s and Tm3s from L1 synapses to T4 synapses and found them to be similar, within 10% of each other. Moreover, utilizing a range of electrotonic parameters measured in other fly neurons[41], the corresponding cable delays were still only on the order of one millisecond, an order of magnitude less than that required for motion detection[32]. Further, although some neurotransmitters have been

identified for the cell types involved, we do not know their associated receptors and hence the resulting synaptic polarity.

In the absence of evidence for both relative delay and synapse polarity, we are free to choose the measurement direction from Tm3 to Mi1, which leads to spatial displacements consistent with the directional preference predicted by the depth of T4's terminal in the lobula plate. Assuming that the Mi1 and Tm3 inputs to T4 are combined with the same sign, as in the HR EMD model[4] (Fig. 1a), we predict that the Tm3 arm of the motion detector should introduce a longer delay than the Mi1 arm. If, however, the inputs were combined with opposing signs, as in the BL EMD model[6] (Fig. 1b), then our prediction would be the opposite. Regarding the mechanism of the delay, having the two arms of the circuit implemented by different cell types allows the possibility that the delay may be implemented biologically by means of metabotropic receptors, as reported in the vertebrate retina[42].

Exploring the reconstructed T4s, we identified a hitherto unrecognized feature of their medulla dendritic arbors (see however T4a,d in Fig. 14 of [21] and Strausfeld N. J., personal communication): the dendritic branches of each T4 neuron are oriented primarily in one direction (Fig. 6a, Methods). Moreover, the branch orientation of each T4, measured from the dendrite tips to their bases, clusters around one of four directions (Fig. 6b). These four directions, when mapped from the medulla's coordinate frame onto the visual field (Fig. 6c), align with the output direction preference for each lobula plate layer (Fig. 6b). This observation allowed us to cross-validate the classification of each of the 16 T4s into direction preference subtypes (Fig. 6a,b, Supplementary Fig. 5). We then used this observation to infer a direction preference for the remaining three T4s, for which tracing into the lobula plate could not be completed (Fig. 6c).

## Discussion

This report has introduced a novel high throughput, semi-automated pipeline for EM reconstruction, and applied it to comprehensively reconstruct a connectome module within the medulla, a neuropil that has long resisted such attempts. Furthermore, using connectomics, we identified Mi1 and Tm3 inputs to T4 neurons as the two arms of a candidate correlation-based motion detector. While anatomy alone does not allow us to probe the nonlinear operation or the time delay, and hence distinguish between different correlation-based models[5,6,43], we were able to predict which cell type should introduce a longer delay, given their synaptic polarities (Fig. 1a,b).

Analogous to our proposed circuit downstream of L1, the connections within our EM reconstruction allow us to suggest candidate cell types – Tm1, Tm2, and Tm4 – that may constitute the motion detection circuit downstream of L2. Confirmation of this suggestion must of course await dense reconstruction of the connections onto T5 neurons in the lobula.

This report has several interesting parallels with results from vertebrate retinas. First, the existence of the four subtypes of T4s responding to the four cardinal directions of motion is reminiscent of the four sub-types of ON-OFF directionally selective ganglion cells (DSGCs) in the rabbit retina[44]. Second, our finding that directional selectivity of T4s is aligned with

their dendritic orientation is reminiscent of JAM-B cells[45] and starburst amacrine cells (SACs)[46]. However, unlike JAM-Bs and SACs, the preferred direction of T4s is away from the tip of the dendrites and, unlike SACs but like JAM-Bs, all dendrites in one T4 point in the same direction. Third, the highly specific connections between SACs and DSGCs responsible for the directional selectivity of the latter were also demonstrated previously using large-scale connectomics[47]. However, unlike the SAC to DSGC circuit, the circuit we report may compute directionally selective responses from non-directional inputs.

Our identification of the candidate motion detection pathway downstream of L1 was greatly aided by the comprehensiveness of our EM reconstruction. Relative to connections estimated by arbor overlap[29], having the precise synaptic counts allows us to unequivocally establish connections (Supplementary Fig. 6). In this way, we identified Tm3 as a primary component of the motion detection circuit, a fact that escaped previous researchers due to its minimal arborization in M10. Further, relative to sparse reconstructions in other systems, e.g. synaptic connections between SACs and DSGCs[47], the comprehensiveness enables us to argue both the absence of alternative pathways and the numerical importance of the proposed pathway.

The significance of the dense medulla connectome also goes far beyond the local motion detector, applying to many other visual computations. While much remains to be done, especially to fully incorporate tangential and infraperiodic cells, our connectome does contain the columnar neurons found in every column and hence removes a longstanding block to understanding insect vision. More generally, our results illustrate that, combined with a rich collection of experimental and theoretical results, connectomes can, by identifying underlying circuits, provide key insight into neuronal computation.

## Methods

### Tissue Preparation, Electron Microscopy, and Imaging

The right part of the brain of a wild-type Oregon R female fly was serially sectioned into 40nm slices. 1769 sections, traversing the medulla and downstream neuropils (Fig. 1c), were imaged at a magnification of 5000x. This process is detailed in the Supplementary Methods.

### Semi-automated Reconstruction Pipeline

To obtain a dense EM reconstruction of the reference column, we used a sequence of automated alignment and segmentation steps, followed by manual proofreading and reconstruction, which we described as the semi-automated reconstruction pipeline[20].

### Image Alignment

We first found a rough alignment of the full image stack, ignoring artifacts such as folds, tears and dirt occlusions, by using TrakEM2 rigid registration[48] to align image blocks consisting of 20 sections of 9 × 9 mosaics, and then aligning blocks by an automated search over images at the center of each mosaic. This rough alignment served to determine which images overlapped, allowing more precise analysis of tissues with artifacts, and in particular, large folds. Pixels much darker than average were assumed to correspond to folds and were

used to divide each image into two or more connected components, called patches. For each pair of overlapping patches, both within a section (along the boundary) and section-to-section, points of correspondence were found by correlation (~1 per 500,000 overlapping pixels). A least-squares fit of these points with regularization for scale and skew was then used to produce a global affine alignment of all patches. Examination of errors from this fit identified images for which the automatic division into patches was inaccurate, and these divisions were corrected manually. Once a satisfactory fit was obtained, each patch of each image was then slightly distorted in order to provide a best match to its neighbor(s) while still remaining close to the global affine. More details are available in the technical report "Automated Alignment of Imperfect EM Images for Neural Reconstruction"[49].

### Automatic Image Segmentation

In the next step, we partitioned the medulla region of interest within the aligned stack of grayscale images into subsets of pixels belonging to individual neurons. Given that the resolution of the TEM dataset is anisotropic, we developed a two-step process comprising 2D segmentation to identify cross-sections of neurons followed by linkage of these segments in 3D. No single algorithm was used on all data, since many different segmentation techniques were tried in parallel with proofreading efforts, and it was counterproductive to re-segment portions already corrected. A typical 2D segmentation step entailed creating boundary probability maps using morphological features[50–52] followed by Boosted Edge Learning[53], mitochondria detection to reduce false boundaries[54], followed by watershed segmentation[55] and agglomerative clustering[56] using mean and median boundary values to create 2D segments. The 3D linkage step constructed a linkage graph of consecutive 2D segments in adjacent sections. Again, several techniques were used, including simple metrics such as overlap, and machine-learning approaches that computed appropriate weights of features from previously proofread data. Further details of some of our automatic segmentation approaches can be found in previous publications[20,57]. Given that all segmentation algorithms make mistakes resulting from imaging artifacts and low z-resolution, and because manual correction of over-segmentations is easier than under-segmentations, we tuned our automatic algorithms to produce an over-segmented image volume. Furthermore, we preserved watershed regions called super-pixels to facilitate the manual correction of over-segmentation in the next step. We have released the latest (and we believe best) version of the segmentation code that we used (https://bitbucket.org/shivnaga/sstem), but caution the reader that even our best automatic segmentation required extensive manual proofreading, correction, and annotation (see below) to yield the results we report in this paper.

### Proofreading/Reconstruction

We next inspected the results of automatic segmentation, corrected remaining errors, and assigned synapses to the proofread cell arbors. Because this was time-consuming, we trained a group of professional editors, referred to as proofreaders, whose work was supervised by two experienced electron microscopists (ST, ST2, PR) (experts). Proofreaders and experts performed their tasks using a dedicated custom software tool, Raveler (Olbris et al., in preparation). In total, these proofreading steps took ~12,940 person-hours (including 900 person-hours contributed by our experts). There were five key steps within the

reconstruction procedure (1) volume proofreading, (2) synapse annotation, (3) postsynaptic tracing, (4) anchor body refinement, and (5) selective sparse tracing, detailed in the Supplementary Methods.

## Reliability of the Wiring Diagram

As introduced above, we assigned two proofreaders to each synapse, to increase the reliability of proofreading. Characterizing this, in 48.2% of cases both proofreaders were unable to identify a parent cell either because they could not trace the process confidently or because it left the medulla region of interest. In 44.0% of cases, both proofreaders traced the PSD to the same anchor body and in 7.5% of cases one proofreader was unable to complete the tracing while the other traced the PSD to an anchor body (numbers extracted from Supplementary Table 1). However, only in very few cases (0.23%) did the two proofreaders reach different anchor bodies. These numbers suggest that a large fraction of connections will be missed, following the two proofreader agreement process; however, all connections that are identified have a very high probability of being correct.

To further assess our reconstruction quality, we generated two connectomes from the dual proofreader results – an inclusive version which included connections found by either proofreader, and a consensus version in which connections were accepted only when both proofreaders agreed. Comparing these two connectomes was generally reassuring. Although the inclusive connectome has ~16% more connections, all the additional connections had only one synaptic contact. All connections with 2 or more synapses are present in both connectomes (Supplementary Table 1). We used the consensus connectome for all our analyses. However, the conclusions remain unchanged when using the inclusive connectome.

In general, the high rates of missed synaptic contacts in our proofreading was tolerable for our project because our intent was to study connections with multiple, parallel synaptic contacts. We could confirm that the connectome contains a large fraction of such strong connections by plotting the distribution of the number of contacts between connected pairs of cells.

We found a strongly heavy-tailed distribution of the total numbers of contacts for each connected pair both in the whole connectome (inset in Fig. 3b), and within the subset of sparsely-traced cell-types involved in motion detection (Supplementary Fig. 3). Given that the sizes of T-bars within the medulla are relatively uniform (McGregor, A. et al., unpublished work) and the size of synaptic structures is thought to correlate with their physiological strength[58], we viewed the number of parallel synaptic contacts between two neurons as a proxy of synaptic weight. Further, making an assumption that the probability of missing a synaptic contact during proofreading is uniform across all postsynaptic sites, we can estimate that the consensus connectome contains all connections with >5 synapses with a confidence level >95% (Supplementary Methods). Therefore we believe our consensus connectome is both precise and comprehensive for strong connections.

### Constructing a Connectome Module

In constructing a repeating module within the medulla connectome, all the members of each class of neurons within the reference column were identified, and the number of synapses from those neurons to all other neurons of the postsynaptic class was averaged over the presynaptic cells. For the ultraperiodic cell types, e.g. Tm3, this could result in a fractional weight. Further, because there are 1.5 Tm3s per column on average, we computed the synaptic weight by multiplying it by 1.5. These fractional weights provide the mean connection strength over different columns, since some columns have only a single Tm3, while others have two.

The directional summation that was used here was chosen because, in our reconstruction, we attempted to proofread each postsynaptic element to its associated neuron. However, we did not attempt to proofread every presynaptic site back to its parent neuron (since some such elements might derive from non-reference columns, which were not densely reconstructed).

This method was modified for the four connections in the motion detection circuit: L1 to Mi1, L1 to Tm3, Mi1 to T4, and Tm3 to T4. In these cases, the number of synaptic contacts from the densely reconstructed medulla connectome was replaced by the number of synaptic contacts identified during sparse tracing of these specific connections (Supplementary Table 3).

### Computing the Mi1 and Tm3 Receptive Field Components

We computed the Mi1 and Tm3 components of the receptive field for each T4, by multiplying the number of synaptic contacts from each L1 neuron to a single intermediate Mi1 or Tm3 neuron by the number of contacts from that intermediate cell to the T4, and then summing over all the Mi1 and Tm3 neurons that receive input from the same L1 (Fig. 4e). This multiplication is equivalent to counting the number of independent synaptic routes from each L1 to each T4, in which each route must utilize a different pair of the synaptic contacts between the L1 and the intermediate target cells, and the intermediate targets and the T4.

### Monte Carlo Error Estimate

Our proofreading methodology results in very few false positive errors, but many false negative errors between neuron pairs (see above). Therefore, it is highly probable that the observed number of synaptic contacts ($m$) is a subset of a higher, true number of synaptic contacts between two neurons ($n$). Assuming that, for any connected pair of neurons each synaptic contact had an equal false negative probability, and utilizing that probability in a binomial distribution, our goal was to estimate the posterior probability, $P(n|m)$ (i.e. probability of the true $n$ given the observed $m$) for different values of $n$. To do this, since the prior distribution over $n$ is unknown, we approximated this posterior probability by the likelihood, $P(m|n)$ (i.e. probability of observing $m$ given some value of the true $n$), for different values of $n$. We generated 1000 different estimates of the true connection weight, for every connected neuron pair, by sampling from the set of possible $n$ values with the computed likelihood given each value of $n$. Neuron pairs that were disconnected because of high false negative error rates were also allowed to connect if their neurite profiles

overlapped in 3D. The number of contacts was estimated using the same sampling method as before (but with *m* equal to zero). In this way, we generated 1000 different connectivity matrices. The displacement was then computed for each matrix. The eigenvalues and eigenvectors of the covariance matrix over all displacement vectors were computed, and used to plot an ellipse along the eigenvector axes with 2σ confidence intervals (Fig. 5a). To extend this construction to the mean displacement over a group of neurons, 1000 variations of the mean were computed, by first sampling from the displacements generated for each neuron, and then computing the mean for each set of samples. The ellipses were then computed, in the same way as before, over this set of 1000 mean values (Fig. 5b, top).

### Effect of Limited Reconstruction Size

Because the spread of the dendritic arbors of the Tm3s connected to a given T4 is greater than that of the Mi1s, Tm3s are more likely to be partially reconstructed, and, hence, missing L1 inputs near the edges of our 19 column reconstruction. To provide a measure of the effect of this cut-off on each T4, we first visually inspected each Tm3 neuron, and classified it into one of four classes, depending on the percent of the arbor that was missing from the 19 column reconstruction. Tm3s which were reconstructed fully received input from an average of 6 L1 neurons. In contrast, Tm3s in the fourth class, which had most of their arbor outside our region of interest, received input from an average of only 2 L1 neurons. By summing up the fraction of L1 inputs missing, weighted by the fraction of inputs provided by each Tm3 class to the given T4, we obtained an estimate of the weighted fraction of L1 inputs missing (through the Tm3 channel) for each T4 (the x-axis in Fig. 5b, bottom). We also used this metric to justify the removal of T4s missing >15% of their weighted L1 inputs (through the Tm3 channel), in constructing the mean responses for T4s with the same output direction preferences (Fig. 5b, top).

### Dendrite Orientation

After proofreading, the T4 arborizations within M10 were skeletonized, starting from the center of the thickest branch, adapting the method of[59] with a modified weighting function. The axonal branch point was determined by ST so as to precisely identify the dendritic part of the medulla arborization. The local orientation around each dendritic node was computed (utilizing three nodes in both directions around each node, and ignoring any nodes with fewer than three adjacent nodes in both directions). The dominant dendritic branch orientation, for each T4 (Fig. 6b), was computed by taking the Fast Fourier Transform[60] of the distribution of orientations across nodes, and defined to be the phase of the fundamental mode component of the transformation. Assuming a normal distribution for the dominant orientation of the cells assigned to a layer (via their axon arbor depth), we computed the probability of each untraced T4 lying within each cluster of cells, given its measured dominant orientation. The assignment of cell T4-4 to layer 1 was significant ($P<0.05$), but the assignment of the other two cells was not. The color map for the dendritic arbors (Fig. 6a, Supplementary Fig. 5) was chosen by centering colors on the average of the dendritic branch orientation for each cluster (Fig. 6b), and varying the color continuously between clusters.

### Data Access

Upon publication the skeletons of all cells will be uploaded to neuromorpho.org. We will also provide the entire segmentation with synapse annotations, along with Raveler to open the dataset, upon request. The requesting party will need to supply a hard drive. We can also provide a software widget for efficiently searching the full connectome spreadsheet.

## Supplementary Material

Refer to Web version on PubMed Central for supplementary material.

## Acknowledgements

We acknowledge the technical support of all members of the Janelia FlyEM project and the Chklovskii group, past and present. We thank S. Laughlin for numerous discussions and M. Reiser for commenting on an early draft of the manuscript. We thank A. Borst, C. Desplan, C-H Lee, T. Clandinin, and L. Zipursky for discussions and granting us access to their data prior to publication.

## References

1. Heisenberg, M.; Wolf, R. Vision in Drosophila. Genetics of Microbehaviour. Springer Verlag; 1984.
2. Laughlin, SB. Progress in Retinal and Eye Research. Vol. Vol. 13. Pergamon Press, Ltd.; 1994. Matching coding, circuits, cells, and molecules to signals: General principles of retinal design in the fly's eye; p. 167-196.Ch. 9
3. Strausfeld, NJ.; Nässel, DR. Neuroarchitectures serving compound eyes of Crustacea and insects. In: Autrum, H., editor. Comparative Physiology and Evolution of Vision in Invertebrates Handbook of Sensory Physiology. Springer-Verlag; 1981. p. 1-132.
4. Hassenstein B, Reichardt W. Systemtheoretische Analyse der Zeit-, Reihenfolgen- und Vorzeichenauswertung bei der Bewegungsperzeption des Rüsselkäfers *Chlorophanus*. Z. Naturforsch. 1956; 11:513–524.
5. Reichardt, W. Autocorrelation, a principle for the evaluation of sensory information by the central nervous system. In: Rosenblith, WA., editor. Sensory communication. MIT Press; 1961. p. 303-317.
6. Barlow HB, Levick WR. The mechanism of directionally selective units in rabbit's retina. The Journal of physiology. 1965; 178:477–504. [PubMed: 5827909]
7. Borst A, Haag J, Reiff DF. Fly motion vision. Annual review of neuroscience. 2010; 33:49–70.
8. Rivera-Alba M, et al. Wiring economy and volume exclusion determine neuronal placement in the *Drosophila* brain. Current Biology. 2011; 21:2000–2005. [PubMed: 22119527]
9. Meinertzhagen IA, Sorra KE. Synaptic organization in the fly's optic lamina: few cells, many synapses and divergent microcircuits. Prog Brain Res. 2001; 131:53–69. [PubMed: 11420968]
10. Takemura SY, Lu Z, Meinertzhagen IA. Synaptic circuits of the *Drosophila* optic lobe: the input terminals to the medulla. The Journal of comparative neurology. 2008; 509:493–513. [PubMed: 18537121]
11. Meinertzhagen, I.; Hanson, T. The development of the optic lobe. In: Bate, M.; Martinez Arias, A., editors. The development of Drosophila melanogaster. Vol. Vol. 2. Cold Spring Harbor Laboratory Press; 1993. p. 1363-1491.
12. Buchner E, Buchner S, Bülthoff I. Deoxyglucose mapping of nervous activity induced in *Drosophila* brain by visual movement. Journal of Comp Physiol A. 1984; 155:471–483.
13. Krapp HG, Hengstenberg R. Estimation of self-motion by optic flow processing in single visual interneurons. Nature. 1996; 384:463–466. [PubMed: 8945473]
14. Joesch M, Plett J, Borst A, Reiff DF. Response properties of motion-sensitive visual interneurons in the lobula plate of *Drosophila melanogaster*. Current Biology. 2008; 18:368–374. [PubMed: 18328703]

15. White JG, Southgate E, Thomson JN, Brenner S. The structure of the nervous system of the nematode *Caenorhabditis elegans*. Philosophical transactions of the Royal Society of London. Series B, Biological sciences. 1986; 314:1–340. [PubMed: 22462104]
16. Kirschfeld, K. The visual system of *Musca*: studies on optics, structure and function. In: Wehner, R., editor. Information processing in the visual system of arthropods. Springer Verlag; 1972. p. 61-74.
17. Riehle A, Franceschini N. Motion detection in flies: parametric control over ONOFF pathways. Experimental Brain Research. 1984; 54:390–394. [PubMed: 6723860]
18. Schuling FH, Mastebroek HAK, Bult R, Lenting BPM. Properties of elementary movement detectors in the fly *Calliphora erythrocephala*. Journal of Comp Physiol A. 1989; 165:179–192.
19. Helmstaedter M, Briggman KL, Denk W. 3D structural imaging of the brain with photons and electrons. Curr Opin Neurobiol. 2008; 18:633–641. [PubMed: 19361979]
20. Chklovskii DB, Vitaladevuni S, Scheffer LK. Semi-automated reconstruction of neural circuits using electron microscopy. Current Opinion in Neurobiology. 2010; 20:667–675. [PubMed: 20833533]
21. Fischbach KF, Dittrich APM. The optic lobe of *Drosophila melanogaster*. I. A golgi analysis of wild-type structure. Cell and tissue research. 1989; 258:441–475.
22. Song S, Sjöström PJ, Reigl M, Nelson S, Chklovskii DB. Highly nonrandom features of synaptic connectivity in local cortical circuits. PLoS Biology. 2005; 3:e68. [PubMed: 15737062]
23. Varshney LR, Chen BL, Paniagua E, Hall DH, Chklovskii DB. Structural properties of the *Caenorhabditis elegans* neuronal network. PLoS Computational Biology. 2011; 7:e1001066. [PubMed: 21304930]
24. Campos-Ortega, JA.; Strausfeld, NJ. Columns and layers in the second synaptic region of the fly's visual system: the case for two superimposed neuronal architectures. In: Wehner, R., editor. Information processing in the visual systems of arthropods. Springer Verlag; 1972. p. 31-36.
25. Blondel VD, Guillaume JL, Lambiotte R, Lefebvre E. Fast unfolding of communities in large networks. Journal of Statistical Mechanics: Theory and Experiment. 2008; 2008:P10008.
26. Eck N, Waltman L. VOS: a new method for visualizing similarities between objects. Adv in Data Analysis. 2007:299–306.
27. Franceschini N, Kirschfeld K, Minke B. Fluorescence of photoreceptor cells observed in vivo. Science. 1981
28. Douglass JK, Strausfeld NJ. Anatomical organization of retinotopic motion-sensitive pathways in the optic lobes of flies. Microscopy Research and Technique. 2003; 62:132–150. [PubMed: 12966499]
29. Bausenwein B, Dittrich AP, Fischbach KF. The optic lobe of *Drosophila melanogaster*. II. Sorting of retinotopic pathways in the medulla. Cell and tissue research. 1992; 267:17–28. [PubMed: 1735111]
30. Bausenwein B, Fischbach KF. Activity labeling patterns in the medulla of *Drosophila melanogaster* caused by motion stimuli. Cell and tissue research. 1992; 270:25–35. [PubMed: 1423522]
31. Strausfeld NJ, Lee JK. Neuronal basis for parallel visual processing in the fly. Vis Neurosci. 1991; 7:13–33. [PubMed: 1931797]
32. Clark DA, Bursztyn L, Horowitz MA, Schnitzer MJ, Clandinin TR. Defining the computational structure of the motion detector in *Drosophila*. Neuron. 2011; 70:1165–1177. [PubMed: 21689602]
33. Joesch M, Schnell B, Raghu SV, Reiff DF, Borst A. ON and OFF pathways in *Drosophila* motion vision. Nature. 2010; 468:300–304. [PubMed: 21068841]
34. Rister J, et al. Dissection of the peripheral motion channel in the visual system of *Drosophila melanogaster*. Neuron. 2007; 56:155–170. [PubMed: 17920022]
35. Schnell B, Raghu SV, Nern A, Borst A. Columnar cells necessary for motion responses of wide-field visual interneurons in *Drosophila*. Journal of Comp Physiol A. 2012:1–7.
36. Tuthill JC, Nern A, Rubin GM, Reiser MB. Contributions of the 12 neuron classes in the fly lamina to motion vision. Neuron. 2013

37. Douglass JK, Strausfeld NJ. Visual motion-detection circuits in flies: parallel direction-and non-direction-sensitive pathways between the medulla and lobula plate. The Journal of Neuroscience. 1996; 16:4551–4562. [PubMed: 8764644]
38. Maisak MS, et al. Directional tuning and layer-specific projection of elementary motion detectors in *Drosophila*. Nature. 2013
39. Srinivasan M, Dvorak D. Spatial processing of visual information in the movement-detecting pathway of the fly. Journal of Comp Physiol A. 1980; 140:1–23.
40. Haag J, Borst A. Recurrent network interactions underlying flow-field selectivity of visual interneurons. The Journal of Neuroscience. 2001; 21:5685–5692. [PubMed: 11466440]
41. Gouwens NW, Wilson RI. Signal propagation in *Drosophila* central neurons. The Journal of Neuroscience. 2009; 29:6239–6249. [PubMed: 19439602]
42. Ashmore JF, Copenhagen DR. Different postsynaptic events in two types of retinal bipolar cell. Nature. 1980; 288:84–86. [PubMed: 6253819]
43. Mizunami M. Synaptic rectification model equivalent to the correlation-type movement detector. Biological cybernetics. 1990; 64:1–6. [PubMed: 2178368]
44. Oyster CW, Barlow HB. Direction-selective units in rabbit retina: distribution of preferred directions. Science. 1967; 155:841–842. [PubMed: 6019094]
45. Kim I-J, Zhang Y, Yamagata M, Meister M, Sanes JR. Molecular identification of a retinal cell type that responds to upward motion. Nature. 2008; 452:478–482. [PubMed: 18368118]
46. Euler T, Detwiler PB, Denk W. Directionally selective calcium signals in dendrites of starburst amacrine cells. Nature. 2002; 418:845–852. [PubMed: 12192402]
47. Briggman KL, Helmstaedter M, Denk W. Wiring specificity in the direction-selectivity circuit of the retina. Nature. 2011; 471:183–188. [PubMed: 21390125]
48. Cardona A, et al. TrakEM2 Software for Neural Circuit Reconstruction. PLoS One. 2012; 7:e38011. [PubMed: 22723842]
49. Scheffer L, Karsh B, Vitaladevuni S. Automated alignment of imperfect EM images for neural reconstruction. arXiv.org. 2013; abs/1304.6034arXiv.org
50. Canny J. A computational approach to edge detection. IEEE Transactions on Pattern Analysis and Machine Intelligence. 1986; 8:679–698. [PubMed: 21869365]
51. Martin DR, Fowlkes CC, Malik J. Learning to detect natural image boundaries using local brightness, color, and texture cues. IEEE Transactions on Pattern Analysis and Machine Intelligence. 2004; 26:530–549. [PubMed: 15460277]
52. Soille, P. Morphological image analysis: principles and applications. 2nd edn. Springer-Verlag New York, Inc.; 2003. p. 316
53. Dollar, P.; Tu, Z.; Belongie, S. Supervised learning of edges and object boundaries. Computer Vision and Pattern Recognition, 2006 IEEE Computer Society Conference on; IEEE; p. 1964-1971.
54. Vitaladevuni, S.; Mishchenko, Y.; Genkin, A.; Chklovskii, DC.; Harris, KM. Microscopic Image Analysis with Applications in Biology. Mitochondria detection in electron microscopy images.
55. Vincent L, Soille P. Watersheds in digital spaces: an efficient algorithm based on immersion simulations. IEEE transactions on pattern analysis and machine intelligence. 1991; 13:583–598.
56. Mohanta, PP.; Mukherjee, DP.; Acton, ST. Agglomerative clustering for image segmentation. 16th International Conference on Pattern Recognition, 2002. Proceedings; IEEE; p. 664-667.
57. Vitaladevuni, SN.; Basri, R. Co-clustering of image segments using convex optimization applied to EM neuronal reconstruction. Computer Vision and Pattern Recognition (CVPR), 2010 IEEE Conference on; IEEE; p. 2203-2210.
58. Kasai H, Matsuzaki M, Noguchi J, Yasumatsu N, Nakahara H. Structure–stability–function relationships of dendritic spines. Trends in Neurosciences. 2003; 26:360–368. [PubMed: 12850432]
59. Sato, M.; Bitter, I.; Bender, MA.; Kaufman, AE.; Nakajima, M. TEASAR: Tree-structure extraction algorithm for accurate and robust skeletons. The Eighth Pacific Conference on Computer Graphics and Applications; IEEE; p. 281-449.
60. MATLAB and Statistics Toolbox. The MathWorks, Inc.; Natick, MA, US: 2012b. Release

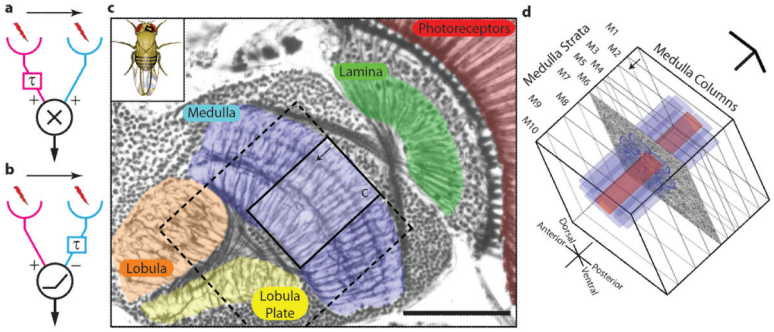


**Figure 1.**

Motion detection and the *Drosophila* visual system. (**a**) Rightward motion component of the Hassenstein-Reichardt elementary motion detector (HR EMD)[4] model. Light input (lightning bolt) into the left channel (magenta) is transmitted with an additional delay, τ, relative to that into the right channel (cyan). For a rightwards moving object, signals from both channels will arrive at the multiplication unit closer in time to each other, and therefore become non-linearly enhanced (and vice versa for leftward moving objects). As a result, the model responds preferentially to rightward motion. (**b**) Alternate Barlow-Levick-like elementary motion detector (BL EMD)[6] model, also preferring rightward motion. Note that the inputs are combined with opposing signs and the delay is now in the right (cyan) channel. (**c**) Bodian silver-stained horizontal section[11] of the *Drosophila melanogaster* visual system revealing the four neuropils of the optic lobe. The medulla region of interest (solid rectangle, expanded in **d**) and the wider imaged volume (dashed rectangle) used to trace into the lobula plate are shown schematically. (**d**) The 37 μm × 37 μm medulla region of interest is centered on the reference column (red) and six surrounding nearest-neighbor columns (blue). The medulla has ten strata (M1-M10) defined by the arborizations of its cell types. Scale bars: (**c**) 50 μm, (**d**) 10 μm (in all 3 directions).

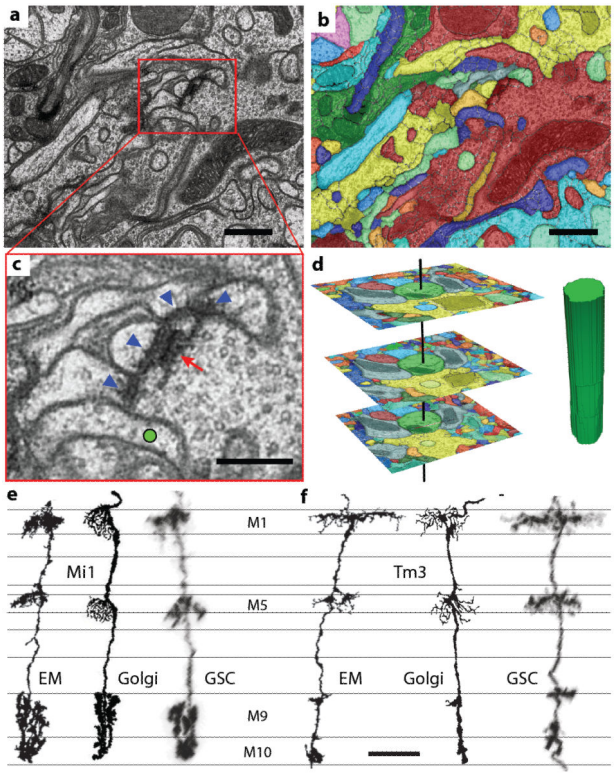


**Figure 2.**

Connectome reconstruction using serial section EM (**a**) A representative micrograph, one of 2769 from the EM series. (**b**) Proofread segmentation of the micrograph in (**a**) into neurite profiles (single colors). (**c**) Synapses comprise a presynaptic process containing a T-bar ribbon (red arrow) and associated neurites with postsynaptic densities (PSDs) (blue arrowheads) adjacent to the T-bar. A non-synaptic process (green circle) lacks a PSD (in both this and other section planes containing this T-bar). (**d**) Neurites are reconstructed by linking profiles in consecutive sections (left), to construct a 3D object (right). (**e**) An example of a neuron reconstructed from EM (left), identified by comparison with the Golgi impregnated cell (center)[21] as type Mi1 and cross-validated by a corresponding genetic single-cell (GSC) labeled neuron (right) (Supplementary Methods). **(f)** Same as **(e)** for cell type Tm3. Scale bars: (**a–b**) 500 nm; (**c**) 250 nm; (**e–f**) 10 μm.

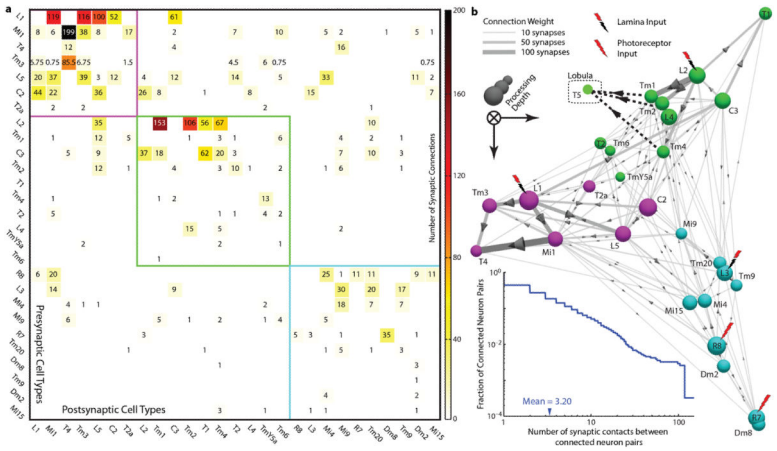


**Figure 3.**

Medulla connectome module. (a) Synaptic connectivity matrix for modular cell types assembled from 2495 synapses (Supplementary Table 1). Three pathways, identified via the Louvain clustering analysis[25], are labeled by colored boxes. They are named by their primary input neuron(s): the L1 (magenta), L2 (green), and L3/R7/R8 (cyan) pathways. The pathways are ordered by the total number of connections within a pathway, in descending order, and the cell types, within each pathway, are ordered by the sum of their pre- and postsynaptic connections to and from other cell types within their pathway, also in descending order. (b) Medulla connectome module as a 3D graph. Cell types with stronger connections are positioned closer to each other, using the visualization of similarities (VOS) layout algorithm[26]. Three spatially segregated groups are observed that closely match the pathways identified through clustering (coloring of spheres). The dominant direction of signal flow is oriented into the page[23]. Inset in (b) shows the fraction of synaptic connections within the full connectome having a connection weight greater than indicated.

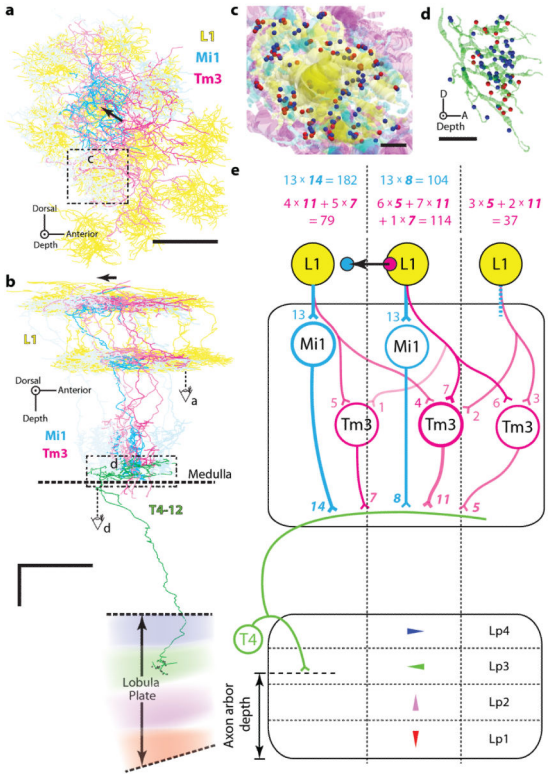


**Figure 4.**

Spatial displacement of Mi1- and Tm3-mediated inputs onto a single T4 (T4–12). (**a**) Bottom view of dendrites of the Mi1 (cyan) and Tm3 (magenta) neurons presynaptic to T4–12, overlaid on the array of L1 axonal terminals (yellow). The color saturation for each dendritic arbor reflects the number of synaptic contacts made onto T4–12 (see (**b, d**)). The arrow shows the displacement from the Tm3 center of mass to the Mi1 center of mass computed as illustrated in (**e**). (**b**) Side view of T4–12 and its presynaptic Mi1s and Tm3s. Direction preference for a T4 (colored to match the directional preferences in (**e**)) is determined by the lobula plate arborization layer of the axon terminals. (**c**) Enlargement (dashed rectangle) from (a) showing reconstructed neurites of Mi1s, Tm3s and L1s (without the weighted colors in (**a**)), and their synaptic contacts (L1 → Mi1: blue; L1 → Tm3: red). (**d**) Reconstructed dendritic arbor of T4–12 with synapses from Mi1s (blue) and Tm3s (red). (**e**) Cartoon of inputs to a single T4 through Mi1s and Tm3s. Mock synaptic weights illustrate how the receptive fields were computed. The center of mass of Mi1 (or Tm3) component, blue (or red) circle, is computed by placing the mass corresponding to the compound synaptic weight from L1 through Mi1 (or Tm3) to T4 at the center of the corresponding column. Scale bars: (**a**) 8 μm, (**b**) 8 μm, (**c**) 1 μm, (**d**) 4 μm.

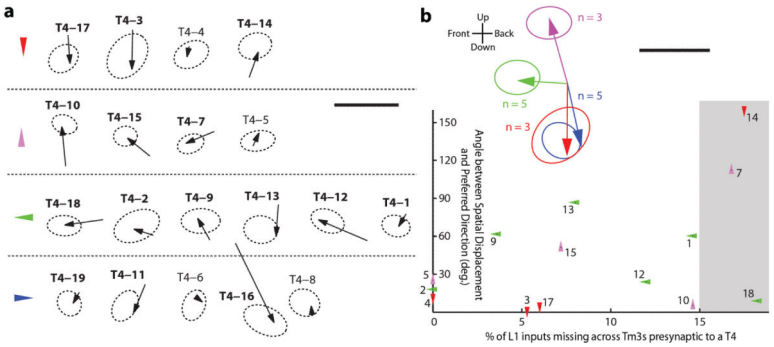


**Figure 5.**

Computed displacements for all T4s (n = 19). (**a**) Displacement vectors for each T4 neuron. Neurons with significant displacement (names in bold) have 95% confidence intervals (ellipses) that exclude the origin (Methods). The vectors are in the ommatidial frame of reference (within ~30° of the visual axes). (**b**) Top: Mean displacement, computed from (**a**), averaged over the cells with the same preferred direction of their output. Bottom: The angular difference between the spatial displacement for individual T4 neurons and the preferred direction of its output (for Lp 1–3) correlates with the fraction of missing L1 inputs (Methods). T4s with >15% of missing L1 inputs were omitted from the mean displacements (top). Scale bars: (**a**) 0.5 and (**b**) 0.2 of the center-to-center distance between adjacent facets.

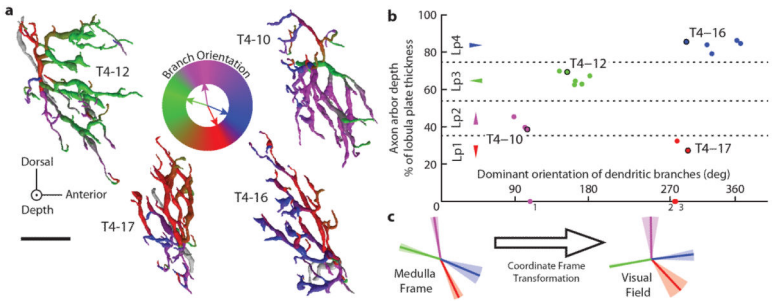


**Figure 6.**

Orientation of medulla dendritic arbors of T4 neurons correlates with axon terminal arborization layer in the lobula plate (as in Fig. 4b,e). (**a**) Four representative medulla dendritic arbors of T4s. The colors represent local dendritic branch orientation. The color map was constructed by assigning colors from each lobula plate layer (Fig. 4e) to the average dominant branch orientation over all neurons in each layer (arrows within color map) and smoothly interpolating. (**b**) Depth of T4 neuron's axonal arbor within the lobula plate correlates with dominant dendritic branch orientation in the medulla (Methods). In the depth axis, four layers are labeled and the neurons within each layer are colored as in Fig. 4e. The dominant orientations of neurons with axons not traced to the lobula plate are plotted on the x-axis (1: T4–5, 2: T4-4, 3: T4–14), and they are colored with the color of the cluster to which they most likely belong (Supplementary Fig. 5). (**c**) Transforming the dominant dendritic orientation (± S.E.M.) from the space defined by the array of medulla columns (in layer M10) to the directions in visual space. Scale bars: (**a**) 5 μm.